CEAS Aeronautical Journal
https://doi.org/10.1007/s13272-026-00954-2

ORIGINAL PAPER

Design and manufacturing of an aileron for a high-aspect ratio wing with active flutter control

Dominic Sahyoun[1] · Yannick Boose[1] · Robert Hein[1] · Nico Liebers[1] · Robert Prussak[1]

Received: 13 March 2025 / Revised: 21 January 2026 / Accepted: 3 February 2026

Abstract

For future passenger aircraft, high aspect ratio wings offer significant fuel savings compared to current models. However, they also introduce a major challenge: flutter becomes a critical issue, requiring the wing to become structurally stiffer and therefore heavier. Active flutter suppression can alleviate this problem, leading to lighter structures and more flexible wings. The aim of the LuFo project WISDOM is to demonstrate an active flutter control system, combined with Maneuver Load Alleviation (MLA) and Gust Load Alleviation (GLA), by actuating the ailerons. This paper focuses on designing the aileron for structural testing, which requires addressing two key challenges: achieving a sufficient stiffness to not dampen the high actuation frequencies and introducing the loads within the small profile thickness. To meet these demands a novel structural concept has been developed for the aileron. Primarely made from Carbon-Fiber Reinforced Polymers (CFRP) Prepreg, this design features a boxed CFRP spar and load-bearing skins, minimizing the need of tooling. The structural design was calculated using finite element and analytical methods. Three ailerons were manufactured in-house at the institute of lightweight systems, utilizing a conventional autoclave process with three negative molds. During manufacturing extensive sensor systems such as Fiber-Bragg-Grating-Sensors, Fiber optical sensors, DC-based cure monitoring sensors and temperature sensors are integrated into the parts and provide valuable information about the behavior of the part and material during the curing process. While the chosen method for joining the separate composite parts is secondary bonding, the design is well-suited for alternative methods like primary bonding or Same Qualified Resin Transfer Molding (SQRTM).

Keywords Structural design · Flutter control · Aileron · Composite manufacturing · Process monitoring

Abbreviations

AR	Aspect ratio
BJSFM	Bolted joint stress field method
CFRP	Carbon fiber reinforced plastic
CG	Center of gravity
CTE	Coefficient of thermal expansion
DC	Direct current
DLM	Doublet lattice method
DEA	Dielectric analysis
FBG	Fiber bragg grading
FCS	Flight control system
FE	Finite element
FOS	Fiber optic sensors
GLA	Gust load alleviation
HAR	High aspect ratio
HIL	Hardware in the loop
HR-FOS	High resolution FOS
IRF	Inverse reserve factor

Yannick Boose, Robert Hein, Nico Liebers and Robert Prussak: contributed equally to this work.

✉ Dominic Sahyoun
dominic.sahyoun@dlr.de

Yannick Boose
yannick.boose@dlr.de

Robert Hein
robert.hein@dlr.de

Nico Liebers
nico.liebers@dlr.de

Robert Prussak
robert.prussak@dlr.de

[1] Institute of Lightweight Systems, Deutsches Zentrum für Luft- und Raumfahrt e.V., Lilienthalplatz 7, 38108 Braunschweig, Lower Saxony, Germany

Published online: 23 February 2026

LCO	Limit cycle oscillations
MLA	Manouver load alleviation
MRCC	Manufacturer recommended curing cycle
PMI-E	Polymethacrylimide
PTFE	Polytetrafluoroethylene
PU	Polyurethane
RTM	Resin transfer molding
SF	Safety factor
SQRTM	Same qualified resin transfer molding
WISDOM	Wing integrated systems demonstration on mechatronics rig
WRBM	Wing root bending moment

Indices

D	Dive
in	Inertia
L	Lower
m	Median
max	Maximum
U	Upper

Variables

α	Angular acceleration
Δc_p	Dimensionless Pressure difference
ϕ	Angle
τ	Shear stress
A	Area
f	Frequency
h	Altitude
J	Inertia
M	Moment
q	Shear flow
V	Speed

1 Introduction

1.1 Motivation

Regardless of the airplane type, a High Aspect ratio (HAR) wing can be a way to significantly reduce emissions by reducing the induced drag of the airplane. The stiffness reduction of HAR wings cannot be compensated only by light weight and high stiffness materials like carbon fibres, which are widely used. Without further provisions, a lower wing stiffness results in lower cruise speeds or the risk of structural damage through gusts, maneuvers or even flutter. Both consequences aren't tolerable in the design of future aircraft and require means of compensation. Gust and Maneuver Load Alleviation (GLA & MLA) have already been implemented in military and civil aircraft in order to reduce the empty weight of the aircraft or to increase the passenger comfort during turbulence [1]. Both alleviation systems reduce the Wing Root Bending Moment (WRBM) and thus the structural weight of the wing [2].

Within the project WISDOM (Wing Integrated Systems Demonstration On Mechatronics Rig) such active means to reduce the loads on the wing are developed. In this case, mainly the ailerons are used to implement those features. Novel manufacturing requirements, a small profile thickness and higher than normal actuation frequencies offer the incentive to come up with a novel structural concept, which unites all requirements.

1.2 Load alleviation and flight controls

A first design choice is to split each aileron into a set of three separate moving surfaces. This is done in order to more accurately control the lift distribution on the wing [3]. This can be done not only for dynamic load alleviation load cases but also for a static optimization of the lift distribution. The primary role of the ailerons remains roll control of the overall aircraft. Additional roll control through the use of flaps is researched in [4] with respect to the researched aircraft configuration. GLA can be implemented by deflecting the ailerons in such a way that e.g. additional lift through a gust can be reduced. A control law for that could be implemented by using a feedback law through the use of sensors on the aircraft structure like accelerometers, angle of attack sensors or other [5] or through a feedforward control law using Lidar to scan for air movements in front of the aircraft [6, 7]. One GLA control system, which will be implemented withing the project is described in [5].

Flutter is an instability in the interaction between an elastic (aircraft) structure and the airflow around its shell. Flutter can occur as Limit Cycle Oscillations (LCO) in which case the oscillations are limited to a certain amplitude. This was experienced during the development of the Boeing 747-8 [8]. In another case, no dampening of the oscillations occur and the amplitude increases until structural failure. This can happen progressively and well predictable, but can also happen suddenly and violent. For this reason, such aeroelastic instability is prohibited up to 1.15 times the design dive speed V_D [9]. An active flutter control system, which shifts flutter to a speed above V_D or above 1.15 V_D is therefore considered safety critical as a failure of the system could lead to structural damage or failure. The flutter control system within WISDOM utilizes aileron deflection to introduce an artificial dampening of critical failure modes. In case of WISDOM a hard flutter mode occurs between 1 and 1.15 V_D, the flutter controller is evaluated through different altitudes at Ma=0.9. An established H-infinity optimization approach is used, 20 accelerometers are distributed over the whole aircraft to measure the structure response [10]. The

controller is able to dampen instabilities at Ma=0.9 across the whole altitude range [10]. A more in depth discussion of the considerations, limitations and the overall structure of the flutter controller is given in [10]. A very in depth review of the current state of the art in active flutter suppression can be found in [11].

Flutter control, GLA and roll control have to implemented in to an Flight Control System (FCS). As stated, this FCS is considered safety critical, not only for primary control, but also secondary control if flutter control is included. An overall description of the implemented FCS is given in [10], a further discussion on safety critical aspects of the FCS is done in [12].

1.3 Manufacturing aspects and design considerations

Through the use of the ailerons for flutter control and therefore higher than usual actuation frequencies, unique design constraints arise for the structural design of the ailerons.

Different structural design thoughts have been implemented in the past in ailerons structural design. Earlier designs rely on a differentiated design with ribs, a spar and the skin each having dedicated load bearing tasks. Those design are made primarily from aluminum alloys. With the advancements in composite materials, aluminum alloys were replaced with composites while the underlying overall design principles still stayed the same. The main advantage was weight savings and a slightly reduced parts count [13]. Today's design methods can better utilize the advantages of orthotropic materials over isotropic materials. This leads not only to further weight savings but also to an integrated design with few parts and complex load distributions between those. One example from research is in [14]. Here a new composite aileron has been designed for the P180 AVANTI aircraft utilizing two main parts which are bonded with structural adhesive. Compared to the differential design of the legacy P180 aileron, a significant reduction in manufacturing effort was achieved by reducing the number of production steps. Limiting the review to only include the structural design of conventionally actuated ailerons wouldn't lead to any further insights. The review is therefore widened to include modern trends in flaps structural design. Here, a similar trend can be observed, with the goal to minimize production steps and part count. Therefore, multispar concepts are proposed utilizing advanced production technologies like Resin Transfer Molding (RTM) or Same qualified-RTM (SQRTM) [15]. In [16] a flap is manufactured using SQRTM consisting of four parts, all manufactured in one mold and one curing cycle. A similar structural design was manufactured from thermoplastic material in [15] with the main benefit of out of autoclave curing. Within the Airbus led composite multispar flap (CMF), a one-shot RTM process was established on an 7.4m outboard flap to reduce the parts count and manufacturing complexity [17]. A reduction of over 20% in manufacturing costs and an integration of originally 26 separate parts into one united structure was achieved. This approach is now used by FACC for the "Wing of Tomorrow" project [18].

In [19] these production based methods are expanded to include a digital twin of the manufactured part. Here, a complex multispar flap is used as an use case scenario for digital manufacturing simulation. Numerous sensor systems are placed within the part and its mold during RTM processing in order to validate a manufacturing simulation. A broader picture is drawn to include this work in an future virtual process from virtual design [20] to manufacturing [21], testing [22] and certification [23].

As can be seen by those examples, structural design of wing moveables is not mainly driven by weight reduction or stiffness, but rather through manufacturing considerations. These include high production rates, reduced autoclave cycles, reduction of manufacturing steps and (although not the focus of the included references) high level of automation.

Apart from production driven design aspects, completely new designs are researched and tested, which break with the thought of discrete, rigid wing moveables. Morphing concepts for moveables have been researched in many projects, although to the authors knowledge no production aircraft has been fitted with such advanced moveables. Notable research on shape variable aileron concepts include [24–27]. Further examples which were tested in large scale flight test programs can be found in [28, 29]. A very in depth review of past and present morphing activities can be found in [30].

1.4 Structure

The publication continues with a description of the configuration and discusses Load Cases, which will be used for sizing and later testing. The novel structural design is described and in Chapter four a load path depended, detailed design considerations are described. Then, calculations and simulation results are described and discussed. In chapter six, the composite manufacturing including the monitoring of the manufacturing process through various sensor systems is explained and manufacturing results and deviations discussed. Finally the work is summarized and an outlook on future works is given.

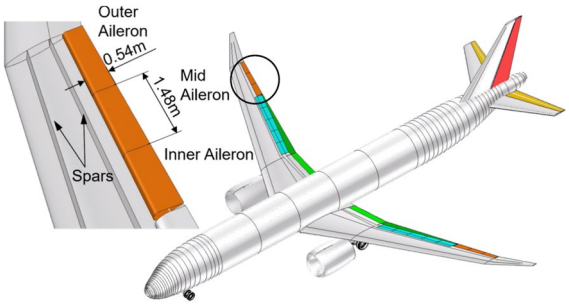

Fig. 1 D2AE configuration with chord and span dimension of the ailerons [31]

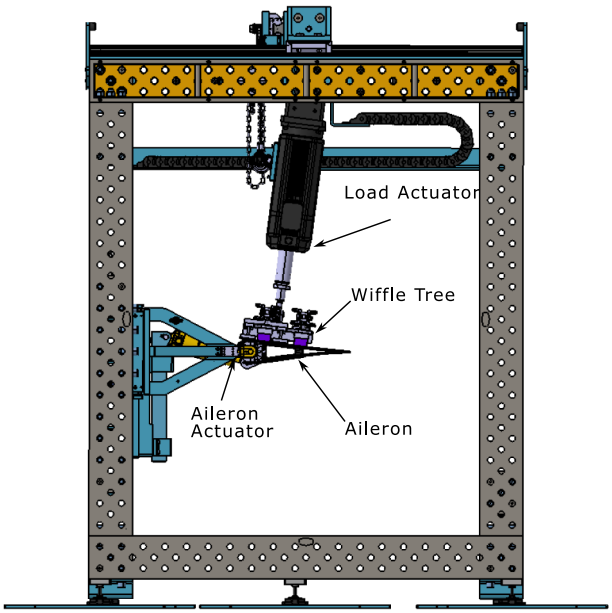

Fig. 2 WISDOM test rig for static loads with load actuator and wiffle tree mounted to the aileron upper surface and the aileron actuator mounted in front

2 Scope within the project and derived loading conditions

Within this project, the existing D239+ aircraft configuration is adapted through the use of a HAR wing with an aspect ratio (AR) of 12.4 and used as a baseline configuration. The wing is designed in such a way, that a predetermined flutter frequency of 6.7 Hz is achieved between the design diving speed V_D and 1.15 V_D [10, 31]. This frequency is a requirement due to the available actuators for the project. Figure 1 shows the resulting D2AE configuration and the moveables of the aileron on one wing.

The demonstration of flutter suppression, GLA and MLA will be shown in a Hardware In the Loop (HIL) test rig. Therefore, individually designed flight computers act together with virtual sensors in the flight model to control the ailerons in the test rig by means of moving the actuators.

Table 1 Boundary conditions for aileron design

Boundary condition	Value	Source
Max. deflection angle	± 25°	D2AE configuration
Max. pos. hinge moment	1242 N m	Aerodynamic calculation
Max. neg. hinge moment	−986.2 N m	Aerodynamic calculation
Deflection at max. hinge Moment	± 12.9°	Aerodynamic calculation
Dynamic actuation frequency	6.7 Hz	Project requirement
Dynamic deflection angle	± 2°	Project requirement
Lever arm actuator	52.4 mm	Kinematics design
Hinge line position	-	D2AE configuration
Max. deformation aerodynamic surface	10 mm	Project requirement
Min. safety factor	1.5	-

The ailerons in return are loaded with the aerodynamic forces, which are approximated through the use of a wiffle tree. The installation of one aileron within the test rig can be seen in Fig. 2.

In the HIL test rig, static load cases up to Limit Load (LL) will be tested. These are the sizing loads for the ailerons structure. Dynamic functional tests will further test the interaction between the ailerons, the aileron's actuator the flight model and the flight control systems.

As visualised in Fig. 1 the complete aileron surface is separated into three sections on each wing. Only the right set of ailerons will be realized and a further simplification is made by manufacturing the middle aileron three times so that only one tool has to be manufactured. Boundary conditions and requirements for the design of the aileron are listed in Table 1 and will be explained in more detail throughout the publication wherever necessary.

3 Structural concept and preliminary design

The aileron contains a highly integrated design which was selected in an early design phase of the project and reflects the aim to reduce manufacturing effort.

3.1 Structural concept

The concept is based on [32], where a new structural design is devised for a flap. There, multiple spars and stringers of current designs are replaced by one large omega shaped spar. A single load bearing skin is attached to the spar in a co-bonding process. Metallic load introduction points are

riveted to the spar and the skin alike. Ribs are therefore eliminated.

This concept is transferred to the aileron and adapted to the unique attachment points and kinematic characteristics of the aileron. Figure 3 shows the evolved aileron concept. Contrary to a flap, the aileron has a wing fixed hinge line which lies inside the clean wing shape, close to the ailerons nose. A single linear actuator is attached to the aileron with a defined offset from the hinge line to facilitate the movement. This results in the attachment points of the aileron to be in front of the spar near the leading edge. According to the described kinematics and attachment characteristics, the initial concept of [32] with the omega shaped stringer was adapted to a box shaped spar with a flat front facing surface (see Fig. 3). This closed profile of the spar additionally increases the torsional stiffness of the aileron greatly.

Another modification of the base concept is the opening within the leading edge. As the aerodynamic load is concentrated near the leading edge (compare with Fig. 6) a closed leading edge would still require stiffeners within the ailerons profile to transfer the high normal loads on the skin to other structural elements. The benefit of a closed profile on the load transfer is therefore not sufficient, as shown in preliminary simulations. As a consequence, one surrounding skin shell with a closed nose was replaced by two separate skin shells with stiffeners in between (see Fig. 3). The opening is defined in such a way, that the skin of the aileron is still sealed to the skin of the wing at the maximum deflection angle.

The spar is the main load bearing element. Aerodynamic loads are transferred from the skin to the spar and then through the brackets to the wing. The spar itself takes the bending loads and provides torsional stiffness for the whole aileron. The open profile of the leading edge is supported through stiffeners and brackets. Those elements are joint with both skins and the spar. Through their stiffness they provide sufficient support for the skin. Peeling of the skins from the spar through the aerodynamic normal loads is hindered through this stiff connection.

3.2 Manufacturing concept

Within the project, prepreg material is used as this material is widely used in the overall aircraft structure of many large passenger aircraft. For the curing process of the parts, three toolings are required, one for the spar and one for each skin. After curing, the parts have to be joined through riveting and adhesive bonding. Another option would be to use a Resin Transfer Molding (RTM) process with a closed tool and three mandrels for the hollow profile sections. Through this process only one autoclave cycle and no secondary bonding would be required. However, prepreg material can't be used for a classic RTM process. Combining the RTM process with prepreg material results in the Same Qualified RTM (SQRTM) process, which unites the advantage of prepreg material with the RTM process. SQRTM could be a way to produce this aileron in a similar way as shown in [15, 16], though its out of scope for this publication.

To preform the box shaped spar, the individual layers of the spar are hand draped around a positive mandrel with the layers forming a stepped joint on the upper surface. The mandrel is then removed and the preform is transferred to the tooling, which is closed afterwards. A tubular vacuum bag is sealed from the inside so that the autoclave pressure is acting on the laminate from the inside of the profile. This process can be seen in the schematic in Fig. 4. A separate manufacturing of the upper and lower half of the spar was ruled out due to a scarf joint or a lap join requiring too much space and conflicting requirements with the attachment of the ribs and brackets.

The skins are manufactured according to a standard process for prepreg material. The layers are layed into the negative molds, a vacuum is drawn and cured within the autoclave.

3.3 Positioning of the novel aileron design within the landscape of existing designs

Current structural design of ailerons for large passenger aircraft rely on a differential design concept. This design method doesn't differ much in terms of their overall structural concept from ailerons made from aluminum. For both the Boeing 787 and Airbus A350 aircraft, ribs and the spar

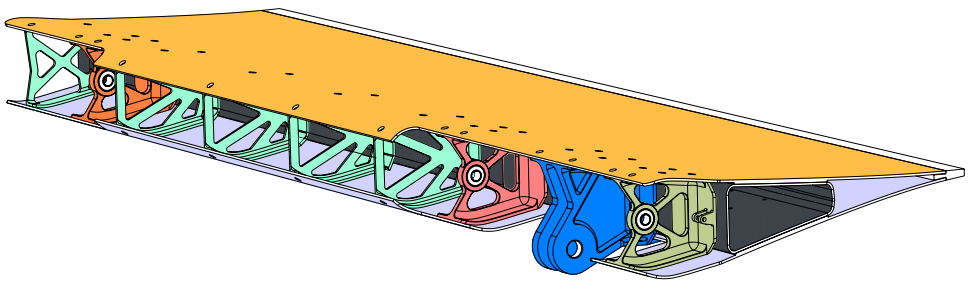

Fig. 3 Colored drawing of the aileron: skin (yellow & grey), spar (black), hinge bracket inboard (light green), hinge bracket center (pink), hinge bracket outboard (orange), jack bracket (blue), stiffeners 1-5 from inboard to outboard (teal), trailing edge (white)

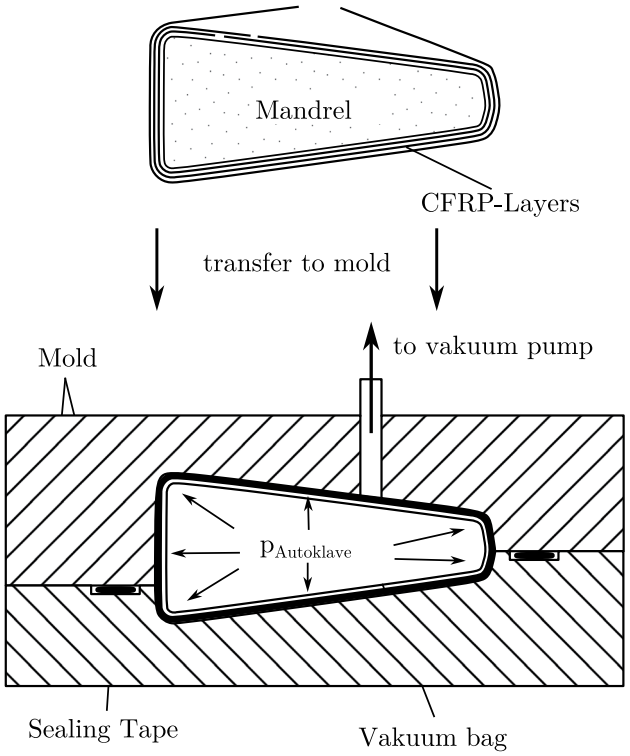

Fig. 4 Schematic for the manufacturing of the spar as seen from its side view

are riveted to a composite skin [33]. Apart from the materials used, this isn't much different to e.g. the aileron of a much older Airbus A320. The parts itself are produced in modern processes like an out-of-autoclave RTM process for the Boeing 787 wing moveables [33]. Many research projects and efforts of manufacturers themselves focus on new structural designs for flaps (see [15–17, 19]). One notable exception of this is done in [14], where the legacy differential design of an aileron is replaced with a modern integrated design, produced within an RTM process. In [13] an aluminium aileron of an Lockheed L-1011 was redesigned to be made out of composite material. This reduced parts count and weight, but it was still an differentiated design, similar in design methodology to metallic ailerons. The new design within this publication is similar in its objectives to [14] and applies the design thoughts for modern flaps onto ailerons. Comparing both designs, the main difference is the closed leading edge in [14], which in this case doesn't need stiffeners to support the profile.

4 Detailed design

Within this section, all design elements and considerations within the design are highlighted and discussed in detail.

4.1 Positioning of hinges and jack brackets

A first design starting point is the number and position of the hinge brackets as well as of the jack bracket, which provides the attachment point of the actuator. The number of hinge brackets largely defines the bending stiffness of the aileron and is itself defined by constraints like a safety critical design and secondary load paths. The position of the brackets defines the bending line under aerodynamic loading. The jack bracket has to be placed as far inboard as possible. This is due to the fact, that the bracket is already protruding through the lower surface due to the low profile thickness. This impact on the aerodynamics has to be reduced.

On each side of the jack bracket, a hinge bracket has to be placed. Under aerodynamic loading the aileron will deform, which has to be kept to a minimum in the vicinity of the actuator attachment. This reduces the risk of jamming of the actuator. Another hinge bracket has to be placed on the outboard side of the aileron. While a stiffness criteria was used in [15, 32] for finding the exact attachment points, here rather than a stiffness criteria, a strength criteria was used. This was done due to not having a strict deformation criteria, and therefore, through optimizing the strength, the weight of the aileron can be reduced.

If compared to the fairly new design of the ailerons of the A350, this concept of the brackets seems viable. The A350 uses two actuators. Therefore one additional hinge bracket is required to place a hinge point on either side of the actuator attachment point. On the far side of the aileron two hinge brackets are placed close to each other [34]. This could be traced back to the requirement to have an additional load path in case of failure. This requirement is not considered in this work though and therefore only one outboard hinge bracket is used. Further research shows that similar connection concepts to the A350 are utilized for other large aircraft as well.

4.2 Use of ribs

Between the brackets, the skins have to be supported to bear the normal loads imposed through the aerodynamic loads. This is done through partial ribs, called stiffeners, which connect the two skins to the spar. Therefore both skins can support each other and the load is transferred to the spar and then to the actuator. Five stiffeners are required to carry the loads without exceeding the stress limits of the skin. In the rear part, no ribs are needed to support the normal loads on the skin. This finding aligns well with other multi-spar concepts in [15, 17, 18]. The main difference to the literature is the opening of the leading edge which is not possible for flaps. Due to the high stiffness of the spar, only the front part

of the aileron has to be supported through stiffeners, while no ribs are required near the trailing edge.

4.3 Design of the trailing edge

For the trailing edge multiple concept could be applied. First, the upper and lower composite skins could be bonded together and form a lip. Next, a honeycomb could be implemented in the trailing edge with the skins bonded to that honeycomb. Last, a metallic strip could be used to attach both skins together.

The first concept does not require additional parts and thus results in a very light structure. Additionally, this concept can be applied to designs with a very small profile thickness. Contrary, the skins need to be thickened to reach a required thickness at the trailing edge. The bonding line of two flat plates requires a deviation of the given aerodynamic profile, which could be a disadvantage of the concept.

A honeycomb structure implements a high stiffness in the trailing edge, while adding only a small amount of weight, which is an important factor considering the lever arm of the trailing edge to the hinge line. This concept was used in [14] and the Airbus A320 outer flap (see [15]). In [19] a foam structure is used with similar structural properties.

Electric charges due to lightning strikes are dissipated through the trailing edge. Therefore those charges would have to pass through the adhesive bonding and impose high mechanical stresses within. A sole adhesive bonding would therefore not be feasible.

It was therefore decided to use a metallic strip for the trailing edge, attaching both skins together. This concept is beneficial, because it does not need an adhesive bonding, adds stiffness with a small weight gain and allows to form the required aerodynamic shape at the trailing edge.

4.4 Connection of different parts

As mentioned in Sect. 3.2 the spar and the two skins are joined by a structural adhesive bonding. This is a necessity of the manufacturing concept as no co-bonding could be used. Therefore, the structural epoxy adhesive EC-9323 from 3 M is used. This adhesive has already been used in-house for the prepreg material, which is described in the next section. The brackets and stiffeners are joined with the spar and skins with blind bolts. These riveted connections can effectively transfer the normal loads on the skin to the brackets and transfer the loads through shear to the spar. Therefore, a load distribution between the riveted connections and the bonded connections is achieved. While the riveted connection take the normal loads, the bonded connection takes the shear flow which results from the deformation of the aileron. The sizing of the connection elements is described in Sec. 5.4f.

4.5 Used materials

Finally a brief summary of the used materials is presented. As the prepreg material, M21E/IMA is chosen due to the institute's extensive experience with its handling and material properties. Additionally, the material has widespread use in the primary structure of current large aircraft models [35]. The layup is chosen through iterative preliminary and final calculations within FEM. Within the skin, the laminate $((0/90)_5/45/\text{-}45)_s$ is derived. At the interface between the skin and the spar this changes to $((0/90)_5/(45/\text{-}45)_2/0_{12}/(90/0)_5)$ with the 0° layers representing the flanges of the spar being the beam. The 0° direction runs in spanwise direction. The layup of the skin could be further refined such as reducing the numbers of layers near the trailing edge and specific strengthening of local load introduction points near the brackets. The spar itself bears the shear loads and therefore consists of a $(45,\text{-}45)_{12}$ laminate.

For the metallic parts, aluminium is chosen. Specifically Al 7075 T6 [36] is selected for every metallic part due to its high tensile strength.

5 Calculations and simulations

In this section detailed calculations and simulations are done to prove that the structure meets the requirements for deformation and Safety Factor (SF) (see Table 1).

5.1 Loads

The loads onto the aileron can be separated into (quasi-) static loads, which arise through aerodynamic maneuver loads, and dynamic loads during flutter control states.

As of the time of sizing of the aileron neither a complete (static) flight envelope nor aerodynamic loads through flutter control states where available. Therefore, assumptions had to be made in order to get loads from the different flight scenarios For static sizing one scenario was found to be critical. CS25 requires a change of roll angle of 60° within 7 s [9]. The aerodynamic loads arising through this requirement maximise for h = 4000 m and Ma = 0.5. An aileron deflection of 12.9° is needed to fulfill the requirement. Aerodynamic loads are given by the pressure distribution on the aileron as well as the resulting Hinge Moment. These loads are listed in Table 2

In case of dynamic loads during flutter conditions, no aerodynamic loads, deflection or deflection rate is known at this point. Therefore project requirements are considered.

Table 2 Specifications of the two investigated load cases

No. load case	Hinge moment	Deflection angle
1	1242 N m	−12.9°
2	−986.2 N m	12.9°

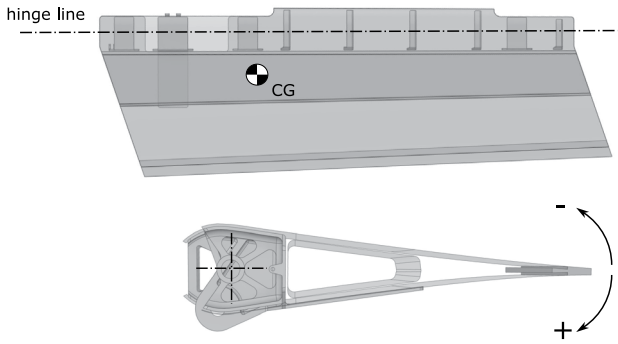

Fig. 5 Control surface with geometric relations of the hinge line, center of gravity (CG) and deflection angle

Here, a maximum frequency of 6.7 Hz and a maximum deflection angle of ± 2° is defined (see Table 1). The assumption is made, that a deflection of only 2° doesn't lead to higher aerodynamic aileron loads, if compared to the much higher deflection during static loading, even at high Mach numbers. This assumption has to be reevaluated, once loads arising through the flutter control are available. In dynamic cases, loads arising through the angular moment of inertia of the aileron should be calculated. Therefore, the inertia around the hinge line of the aileron was measured. This was done by measuring the mass of the aileron, the center of gravity and the Eigenfrequency while rotating the aileron around its hinge line. By considering the relations of a compound pendulum the inertia can be calculated as follows [37]. The associated geometric relations are displayed in Fig. 5.

During a flutter control case, the aileron is moved through its maximum dynamic deflection range with its maximum frequency. A maximum angular acceleration can then be calculated to

$$\begin{aligned}\alpha_{\max} &= \max(-4\pi^2 \cdot f_{\max}^2 \cdot \phi_m \cdot \sin(2\pi \cdot f_{\max} \cdot t)) \\ &= \max\left(-4\pi^2 \cdot \left(6.7\frac{1}{s}\right)^2 \cdot 2° \cdot \frac{\pi}{180°} \cdot \right. \\ &\quad \left. \sin\left(2\pi \cdot 6.7\frac{1}{s} \cdot t\right)\right) \\ &= 61.9\frac{1}{s^2}\end{aligned} \tag{1}$$

Finally, the resulting hinge moment results to

$$\begin{aligned}M_{in} &= J \cdot \alpha_m \\ &= 0.60\,\text{kg m}^2 \cdot 61.9\frac{1}{s^2} = 37.1\,\text{N m}\end{aligned} \tag{2}$$

This moment is considerably smaller than the moments arising through static loading of the aileron and can therefore be neglected (see Table 2). Nevertheless, dynamic loads influence the design. It is still necessary to minimize the inertia so that loads on the aileron actuator are kept small. This, as well as well as overall aircraft considerations, require the weight to be kept minimal. The two resulting load cases with their respective hinge moment are listed in Table 2.

5.1.1 Fitting of the aerodynamic loads

The aerodynamic loads are calculated through a Doublet Lattice Method (DLM) on 35 points on the aileron (see [38] for description of used methods). Apart from a hinge moment, this method produces values for Δc_p in the chamber line of a profile. Δc_p is defined as

$$\Delta c_p = \frac{c_{PU}}{c_{PL}} \tag{3}$$

with c_{PU} being the pressure coefficient on the upper profile surface and c_{PL} on the lower surface respectively. Therefore no information could be gained regarding the absolute pressure on each surface. The decision is to divide the hinge moment in equal parts and apply this on each data point. With the information of each point's lever arm an absolute force is calculated. In order to utilize the pressure distribution, each force is then weighted by the corresponding Δc_p value. The resulting force distribution is then representative of the results of the aerodynamic calculations. For better mapping capabilities within the FE program, each force is converted to a pressure with the help of each points surface area within the aerodynamic calculations. These steps are done for the two load cases.

5.1.2 Mapping of the aerodynamic loads within ANSYS

The resulting loads are imported and mapped by ANSYS to the mesh. This is done program internally by transferring data from one mesh to another mesh [39]. The way this transfer is done can be controlled by user input. In this case, the meshing could only be done very poorly, as an aerodynamic mesh with 35 nodes has to be mapped to a FE-mesh with a few thousand nodes. Figure 6 shows the mapping result for one load case and the coarse pressure distribution reveals the low number of aerodynamic pressure positions. As seen in Fig. 6 a large gradient in the pressure distribution can be observed near the leading edge.

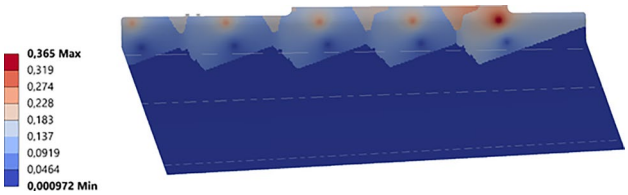

Fig. 6 Pressure distribution of maximum negative deflection mapped within ANSYS on the FE-mesh

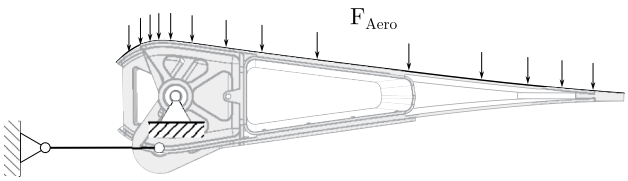

Fig. 7 Mechanical boundary conditions for calculation within ANSYS

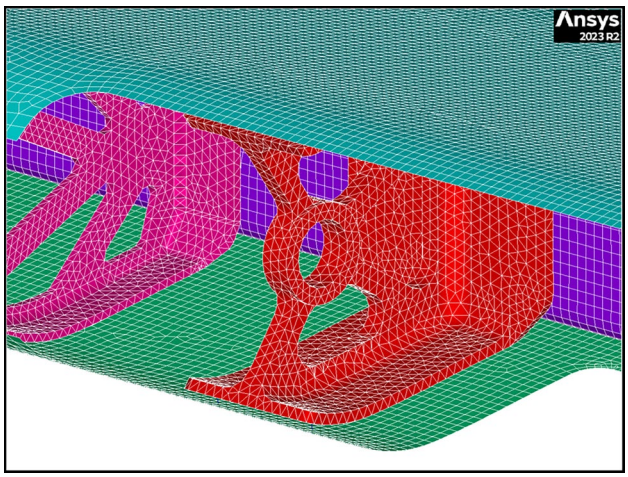

Fig. 8 Detail of mesh around one hinge bracket shown within ANSYS

A validation of the mapping can be done by inverting the mapping from the FE-mesh back to the aerodynamic data points. This results in a maximum deviation of around 30%, located in the data points which are just behind the leading edge. The likely cause for this deviation is a combination of the large gradient in the pressure distribution and the coarse mesh. This deviation is quite high, but couldn't be reduced by changing the mapping settings. The hinge moment within the program can be compared to the input data. An increase of 24% resp. 15% for both load cases of the hinge moment can be observed, when compared to the aerodynamic loads. Therefore, the overall calculation can be considered conservative, but should be further improved.

5.2 Description of ANSYS model

The mechanical boundary conditions within ANSYS are done as shown in Fig. 7. The aileron is free to rotate around a wing fixed hinge line. The three hinge brackets form the support for the aileron and limit any translational movement. Within the ANSYS model the actuator is strongly simplified as a hinged beam. Through this beam the majority of the aerodynamic forces are transferred to the support. Within ANSYS this beam is represented as a joint, which can move in profile thickness direction and in the direction of span, but movement in chord direction is omitted. In order to have a kinematically and statically determined system, movement in the direction of span is hindered at the inboard hinge and is free in both other hinges.

For the spar and both skins, the laminate is defined within the module ACP Pre. It is then transferred to the mechanical system as a shell, as the laminate is sufficiently thin. The shell elements are meshed with SHELL181 linear elements, all solids are meshed with SOLID187 quadratic elements. As seen in Fig. 8, the skins and spar are meshed with a quadrilateral mesh while the solids are meshed with an tetrahedral mesh with an element size of 4 mm.

The bonded connections are implemented as a bonded contact with the Augmented-Lagrangian method. The riveted connections between the composite parts and the brackets or stiffeners are simulated with an MPC184 rigid element for each blind bolt. As preliminary simulations have shown, significant intersection between the skin and the brackets' surfaces occurred due to the deformation of the skin. Therefore a no friction contact with separation was placed between each face of the solids and the shells. This contact only transmits pressure loads on the contact surface.

5.3 Results

In the following sections, the results of the detailed FE analysis are shown for each load case.

5.3.1 Deformation

Figure 9 shows the upscaled deformation for load case one and two. For both load cases torsion and bending is visible with bending deformation being dominant. A maximum deformation of 6.6 mm is observed under load case one, which is within the requirements (see Table 1. Due to the higher absolute hinge moment in load case one, the deformation is higher there. The highest deformation is occurring near the trailing edge even, at the leading edge significant deformation is occurring as well. Rotation about the hinge axis is allowed and due to the statically determined system, limited to the effects of the deformation. A maximum rotation of around 1° is observed in load case one at the outboard hinge bracket.

Figure 10 focuses on the bending of the aileron and in particular of the spar during the first load case. Within the bending line of the spar, no bending is observed between

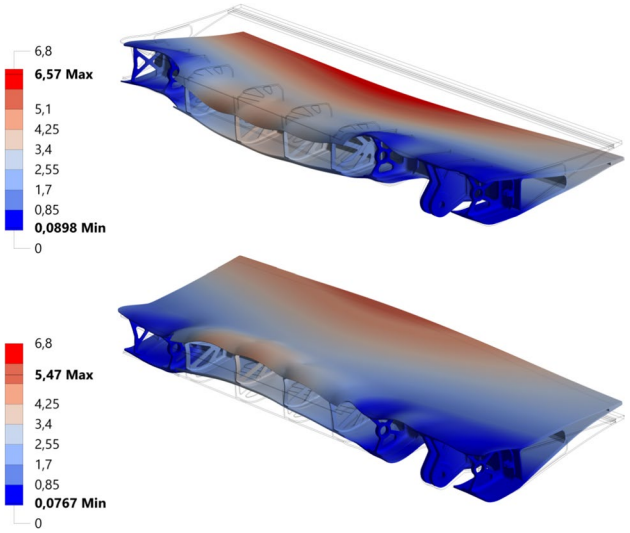

Fig. 9 Global deformation for both load cases (scaled 12 times) in mm

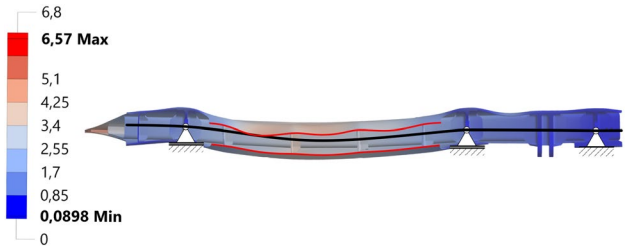

Fig. 10 Global deformation for first load case seen from front in mm (scaled 12 times) with the approximate bending line of the spar shown in black and the deformation of the leading edge skins in red

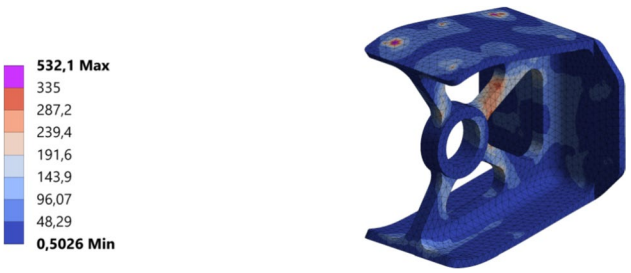

Fig. 11 von Mises stress on center hinge bracket in MPa

the inboard and center hinge bracket. The highest bending is observed between the center and outboard hinge point. The highest curvature is right after the center hinge point and therefore the highest stresses are expected here. The stiffeners and brackets transfer the load from the upper skin to the lower skin, as both skins describe a similar bending line. Between the stiffeners a higher bending mode is observed in the upper skin but not in the lower skin.

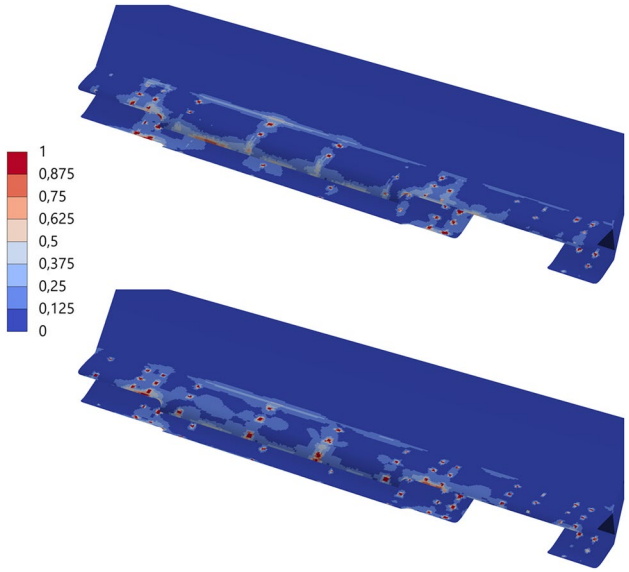

Fig. 12 Inverse reserve factor of the skins during load case 1 (upper) and load case 2 (lower)

5.3.2 Equivalent stresses

Equivalent stresses for all solid bodies are given as von Mises stress. Within this paper, only one relevant and exemplary bracket is shown. The center hinge bracket is the most stressed bracket, which is shown in Fig. 11. This occurs during the first load case. The maximum yield stress of the material Al 7075 T6 including the safety factor of 1.5 is at 335 MPa [36]. This yield stress is exceeded only very localized at the rivet points. There the rigid MPC184 rivet element acts on a single node, which leads to high local stresses. Therefore, those points are ignored. Apart from this the highest stress is at 319 MPa within one of the struts (see Fig. 11). All brackets experience their highest stresses during the first load case.

5.3.3 Composite failure

The failure of the composite parts is evaluated with a 2D Puck Criteria. As seen in Figs. 12 and 13, the Inverse Reserve Factor (IRF) is below the required value of IRF = 0.67 at those elements, which are in contact with the rigid beam elements for the rivets. This is expected and therefore this failure is not considered here. For both load cases, an increased IRF is observed in the skin at the edge of the spar. This is a result of the change in stiffness of the overall aileron. During both load cases, the leading edge of the upper skin experiences failure with a IRF of about 0.7. Here the outer 0° layer experiences matrix failure (Puck Mode A) due to the high curvature of the skin. This could be also attributed to the free edge effect [40].

Fig. 13 Inverse reserve factor of the spar during load case 1 (upper) and load case 2 (lower)

The spar experiences its highest IRF directly next to the center and outer hinge brackets under load case 2. As already discussed, this is due to the change in curvature in the bending line (compare also Fig. 10). High IRF also occurs during both load cases at the position of the outboard bracket due to high shear forces introduced into the laminate there. The highest IRF can be generally observed in the radii. Overall, no failure can be observed in the spar.

5.4 Calculation of rivet failure

The forces on the MPC184 elements in the FE model are used to calculate the rivet failure. For this, the forces are extracted and transformed so that a resulting tensile force and shear force is obtained. These forces are then compared with the allowable tensile and shear forces from the manufacturer of the rivets. The ratio of simulated force to allowable force gives the SF. The maximum tensile force on one rivet is at 3606 N resulting in SF of 1.67. This rivet is located on the lower part of the fourth stiffener. The corresponding load case is load case 1. As the aerodynamic force is pulling on the upper skin and therefore on this rivet, this seems reasonable. All other rivets, which connect the upper skin with the stiffeners are highly loaded as well but don't see such high loading.

The highest shear force of 5519 N results in SF of 1.88. This occurs under load case 1 on one of the rivets connecting the lower skin to the center hinge bracket (compare also Fig. 11). This is likely due to the proximity to the corner of the opening of the lower skin for the jack bracket paired with the high shear due to the change in curvature on that position. In general, the rivets connecting the brackets and stiffeners with the spar are the highest shear loaded rivets. This is by design and confirms the assumptions for the load path within the parts. Again, all rivets of the center hinge bracket are highly loaded with shear due to the change in

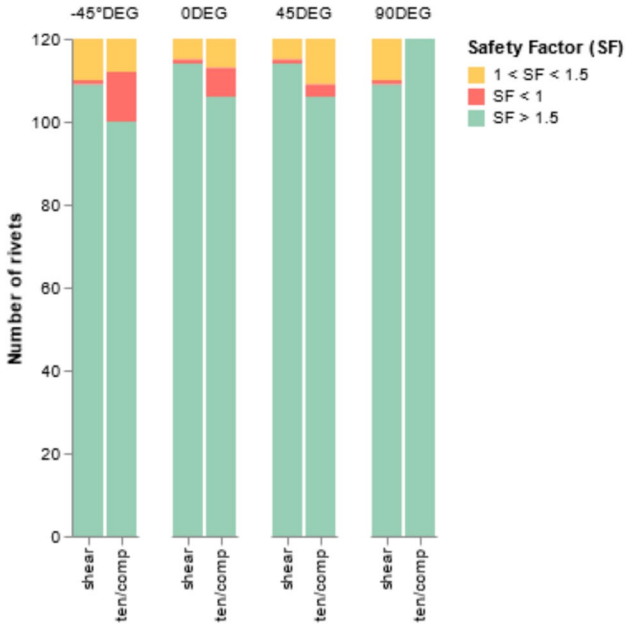

Fig. 14 Failure of plies, broken down by ply direction and failure mode (tension/compression or shear)

curvature in the bending line. This is more pronounced in the first load case as the forces are higher.

The stresses and strains in the vicinity of each rivet are calculated through the Bolted Joint Stress Field Method (BJSFM) [41]. This program uses Lekhnitskii's work on the computation of stresses and strains around loaded holes in laminated plates [42] and relies on the superposition of bypass and bearing loading. The composite failure is analyzed via the maximum stress failure theory. In order to obtain the bearing load, forces at the MPC184 are transferred to the BJSFM program. For the bypass loads, stresses in the vicinity around each rivet are extracted from the FE-Model and then the mean value is entered to the BJSFM program. Results are calculated at 100 points in circumference direction and at 100 points in radius direction. The evaluation of composite failure is done at 10 points around the circumference of the hole with a distance to the hole rim of 10% of the hole diameter. As countersunk rivets are used, a mean effective diameter is used as described in [43].

At a significant number of rivets the composite shows failure during both load cases. In Fig. 14 the results are shown for load case 1.

At most rivets, the -45° ply fails in tension or compression. Those rivets connect the center and outboard hinge bracket as well as the stiffeners in between those brackets to the upper and lower skin. The laminate of the skins is mostly made out of 0° and 90° plies and only four ±45° plies. As the load is mainly transferred by shear around the holes, more ±45 ° plies should be added to the laminate in the vicinity of the rivets. The laminate around a few rivets fail, which

connect hinge brackets and stiffeners to the spar. Here the failure mode changes from rivet to rivet and can be mostly attributed to the high shear loading of the rivet itself which then can't be transferred to the laminate.

Load case 2 shows similar results, albeit with laminate failure around different rivets due to the opposite load direction.

5.5 Calculation of bonded joints

The bonded joint between the spar and the two skins is calculated analytically. As a conservative assumption the whole hinge moment M_{Hinge} has to be transmitted as shear through the bonding. The bonding itself consists of four separate bonding joints on each of the bonding surfaces to minimize the stress increase at the edges of the bonding.

According to Bredth-Batho [44] the shear flow q results to

$$q = \frac{M_{Hinge}}{2 \cdot A_m} = \frac{1242\text{N m}}{2 \cdot 7420\text{mm}^2} = 84\frac{\text{N}}{\text{mm}} \tag{4}$$

with A_m being the enclosed area by the spar. The shear flow is assumed to be equally transmitted by the eight bonding positions with four between upper skin and spar as well as for between lower skin and spar.

To calculate the stresses within the individual bonding a literature approach by [44] is used. This method is based on an analogy to the sandwich model presented in the same work and is able to consider joining of two different materials with different thickness. Elastic characteristics of the joint parts and the adhesive is considered.

Based on general elastic theory, the shear stress within each adhesive layer results to $\tau_m = 14.6$ MPa. Considering the elastic peaks within the adhesion layer, the maximum shear stress at each edge is $\tau_{max} = 17.7$ MPa. This includes the bonding thickness of 0.5 mm, the length of 15 mm and the shear modulus of the adhesive of 2 GPa. As no information about the elastic properties of the adhesive was available, this relatively high and therefore conservative value is chosen. With $\tau_{allowed} = 28$ MP, obtained by the data sheet of the adhesive, this results in a safety factor of 1.61.

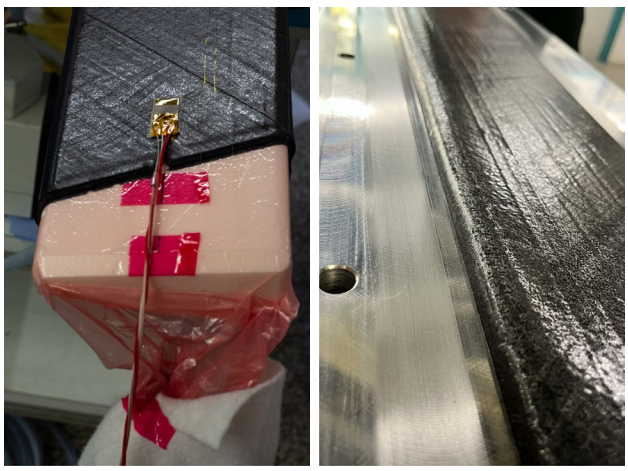

(a) (b)

Fig. 15 **a** Plies wrapped around the mandrel after compaction with the curing sensor. **b** The finished preform placed in the bottom mold half

6 Composite manufacturing

This chapter gives an overview of the composite parts of the ailerons. As the skins are nearly flat sheets, the manufacturing is straight forward. Therefore, the emphasize is put on the spar manufacturing. All three ailerons are manufactured with the same manufacturing process without major modifications in between those.

6.1 Manufacturing of the spars

Each ply of the spar is designed in CAD and cut on a machine. As described in Sect. 3.2, the plies are first placed around a mandrel. This mandrel is manufactured out of a closed cell PMI-E foam. If necessary, the mandrel material allows a destructive removal after the preform is formed. Around the mandrel a tubular vacuum bag is placed. The individual plies are hand draped around the mandrel (see Fig. 15a). On the top side the plies connect in a butt joint, which gets offset by 20 mm for each ply. Every four layers, the stack is compacted with vacuum and with additional 0.5 bar of pressure from the outside. The mandrel is then removed from the preform. This step is relatively easy done by a few knocks onto the mandrel. The preform is stiff enough to support itself and can then be transferred into the still open mold (see Fig. 15b).

To ensure a proper vacuum, sealing tape is applied between both tooling halves. The mold is then closed and the vacuum bag sealed. A gap of around 0.1 mm between the front side of the preform and the mold is noticed. In thickness direction a larger gap of around 0.5 mm is observed. The corners are the most critical part for the fit between the mold and the spar. Here an even larger gap can be seen. While all other gaps are closed if vacuum is drawn, the gap in the corners remains in place. This is further facilitated by a difficulty of the vacuum bag applying pressure in the corner. For future manufacturing, this could be mitigated by the use of pressure strips made of silicone, but this use should be carefully considered as this could lead to ondulations within the radii [45].

After curing the flat surfaces of the spar don't show any defects on the inside or outside, as seen in Fig. 16. The

(a) (b)

Fig. 16 **a** Inside of the spar is shown with no visible surface defects. **b** One corner of the spar is shown with surface defects in the corner

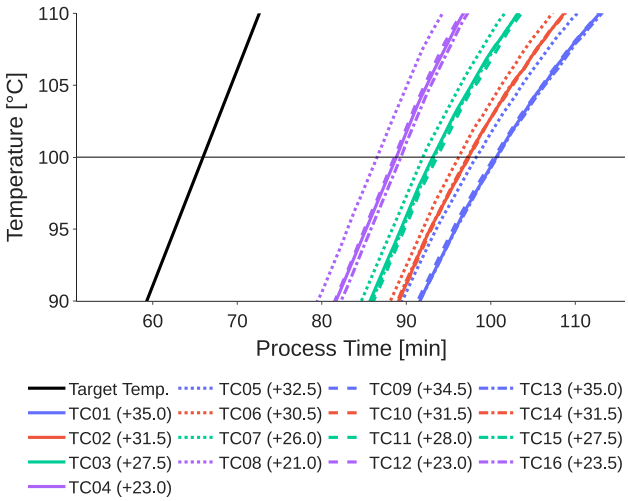

Fig. 17 Measured temperature by tool mounted thermocouples (delay in [min] to reach 100 °C in reference to the autoclave target temperature)

corners clearly show, that there was no contact between the mold and the spar (see Fig. 16b

6.2 Monitoring of the manufacturing process

During the manufacturing of each spar, different sensor systems are integrated into the layup for monitoring different parameters during the autoclave cycle. These sensor systems are Fiber Optic Sensors (FOS), temperature sensors and a DC-based cure monitoring system.

6.2.1 Temperature measurement

The temperature is measured by type J thermocouples in a metal sheath which are integrated into blind holes in the tooling allowing measurement about 2 mm close to the inner surface. For data acquisition the autoclave integrated interface, hardware and software is used. On each tool side (top, bottom, leading and trailing edge) at the same position four thermocouples are mounted over the length with a distance of 367 mm between each position resulting in an equally spaced layout.

In Fig. 17 a detail of the temperature measurement result is shown along the target autoclave atmosphere temperature. To analyze the temperature distribution inside the tooling, a representative target temperature of 100 °C is chosen at the delay between the target temperature and each thermocouple measurement result is determined. The regarded delays are in a range between 21 and 35 min depending on the position. Thermocouples TC04, TC08, TC12 and TC16 are closest to the autoclave door, where the circulating autoclave air is introduced into the inner chamber and reach the target temperature first as this is the area of highest turbulence and thus highest heat transfer coefficient. At the opposite positions TC01, TC05, TC09 and TC13 the temperature delay is most pronounced, where the gas stream has cooled down. On the tool top side at thermocouple positions TC05 to TC08 the delay is slighlty less considerable and on the other sides almost equal. In the next section a cure model is used to estimate the resulting delay of the degree of cure evolution between the hottest and coldest tool spot.

6.2.2 Cure modeling

The temperature measurement results are used as input into a cure model for comparing the cure progression at both locations of smallest (TC08) and highest (TC01) temperature delay. The cure model published in [46] for M21E was used and the results are shown in Fig. 18.

During the first heat ramp to reach 140 °C only negligible curing is occurring and hence the temperature delay has no effect. During the holding dwell at 140 °C the resin cures to about 47% at position TC08, while due to the delayed temperature rise at position TC01 the cure is delayed about 30 min. During the second heat ramp and holding dwell at 180 °C the temperature and cure delay is slightly less pronounced as the heat ramp is shorter (40 K) and the temperature difference is equalled faster. During the holding dwell at both positions complete cure is reached. A more comprehensive cure and also a deformation modeling will be published in a separate paper.

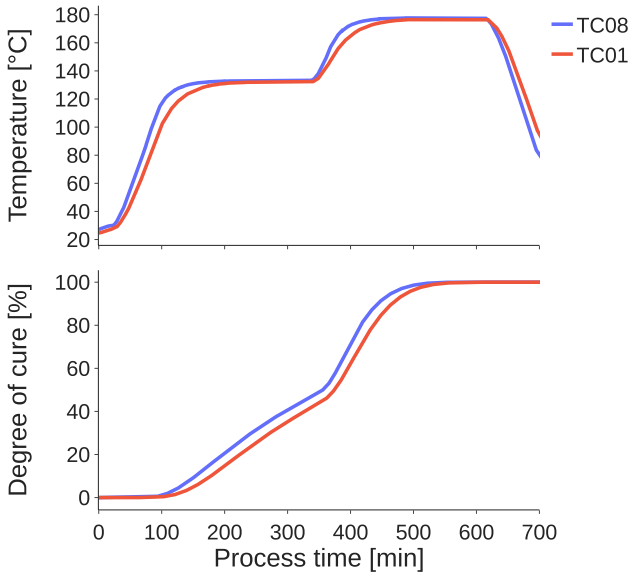

Fig. 18 Degree of cure calculated from tool temperature measurement

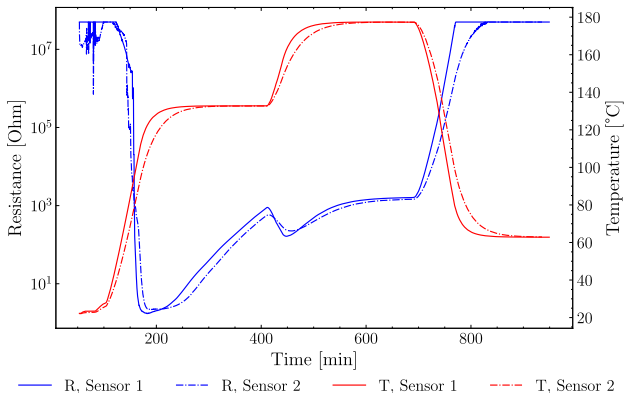

Fig. 19 Measured resistance and temperature of both sensors

6.2.3 Cure monitoring

The cure monitoring system from Synthesites measures the electrical resistance and temperature of the resin, which can be used for estimation of the degree of cure. Figure 19 depicts the measured resistance and temperatures of the two sensors. These sensors are placed at both inboard and outboard edges (see Fig. 15a). At the start of the curing process, the temperature rises to the first dwell phase. As a result, the resistance decreases due to the reduced viscosity of the resin. The signal then increases during the first dwell phase as the viscosity increases due to cross-linking reactions. During heating to the final cure temperature, the resistance drops first and then rises again. The drop is caused by the temperature dependence of the resistance. The signal is superimposed by an increase in viscosity due to further cross-linking reactions. Before cooling begins, saturation can be observed, indicating that the material is fully

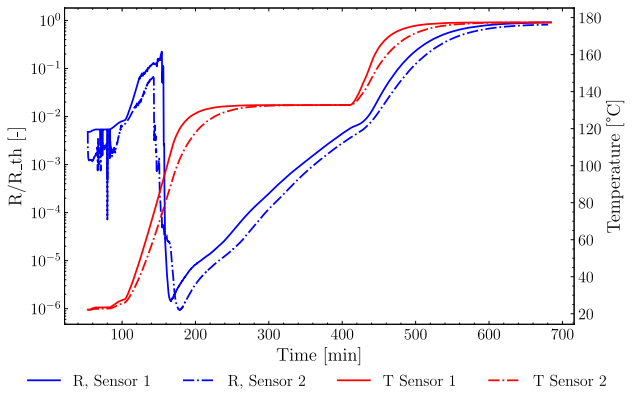

Fig. 20 Temperature compensated resistance and temperature of both sensors

cured. The resistance continues to increase during the cooling phase due to the temperature dependence. The graph shows that the measured resistance signal depends on both the temperature and the cross-linking reactions. To obtain a monotonically increasing signal, temperature compensation is performed by dividing the signal by the resistance of the fully cured material during the cooling phase. The temperature compensated signal is shown in Fig. 20. The graph now indicates a monotonically increasing signal which can be used for cure monitoring. A correlation of the resistance with the fiber bragg signal shown in the next subsection as well as with a process simulation is in preparation and will be published in a separate paper.

6.2.4 Integration of the fiber optic sensors during laminate manufacturing

To monitor the strain evolution during the curing process, two types of fiber-optic sensors were embedded between the two outer layers of the spar's laminate bottom panel:

1. Fiber Bragg Grating (FBG) sensors contain photo-written gratings (spread of a few millimeters) in the core of the optical fiber, enabling the measurement of local strain at specific points.
2. Optically distributed measuring sensors (High Resolution FOS (HR-FOS)) with an ultra-high spatial resolution of 1,538 gages per meter for measuring along the whole length of the sensor fiber and the spar.

Both sensor types are based on a single-mode silica glass fiber with a polyimide coating and a diameter of 0.155 mm. The FBG sensor data is acquired using the Optical Sensing Interrogator HYPERION Si255, while the HR-FOS sensors are analyzed with the Optical Distributed Sensor Interrogator LUNA ODiSI 6100 Series.

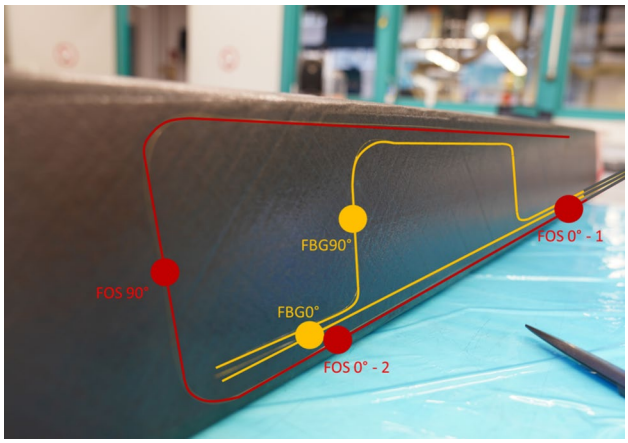

Fig. 21 Positions of the evaluated measurement positions of the integrated fiber optic sensors

One FBG fiber is aligned longitudinally to measure strain in 0° direction, while another fiber follows a meandering pattern to capture strain in the 90° direction. Each fiber contains a single measurement point (Fig. 21). The high-resolution fiber-optic sensors (HR-FOS) run parallel to the longitudinal FBG fibers, providing a continuous strain profile along the entire spar length. Additionally, a section is oriented in the 90° direction as well (Fig. 21). This parallel layout allows for a direct comparison of strain values between the FBG and HR-FOS sensors at the locations of the FBG gratings. To ensure comparability, only localized measurement points from the HR-FOS data are considered.

Outside the laminate, the integrated sensor fibers were protected by a PTFE tubing. The jacketed fibers were then routed through an airtight feedthrough in the autoclave wall and connected to the measurement systems, enabling real-time strain monitoring throughout the autoclave curing cycle.

6.2.5 Collected data from autoclave curing process

The CFRP spar including the fiber optic sensors was cured in an Autoclave-MRCC. During the curing process, the following data (Fig. 22) was collected. The plot illustrates the sensor signal at three different HR-FOS positions (see Fig. 21) over the duration of the curing cycle, alongside the temperature profile of the process. The temperature data was recorded at both the front and the rear end of the spar laminate. Due to unknown thermal influences on the signal in detail, only the signal shifts that correlate with the non-temperature-compensated strain values are considered. Therefore, the following discussion focuses on the qualitative behavior of the measurements and noticeable features.

Signals from fibers at positions 1 and 2 reveal a delay in the signal propagation along the spar length. This is due to the asymmetric heating of the autoclave, where the front heats up faster than the rear. Generally, the strain behavior in the 0° direction appears to be strongly correlated to the temperature, as the prepreg expands along its length together with the aluminum tooling.

The strain in 90° direction at position 3 is proceeding differently. At the beginning of the cycle, the laminate is compacted and pressed into the outer negative mold, leading to an initial expansion. This results in high strains (local peak) within the uncured but highly viscous laminate (see green line in Fig. 22). As the temperature increases, the matrix liquefies, reducing shear forces between the laminate and the sensor fiber, which in turn leads to slippage at the contact interface. Consequently, a decrease in elongation is observed.

During the second heating phase, a local strain maximum is detected (see green line in Fig. 23). The rising edge of the signal can be attributed to increasing temperature and, consequently, laminate expansion. The subsequent drop

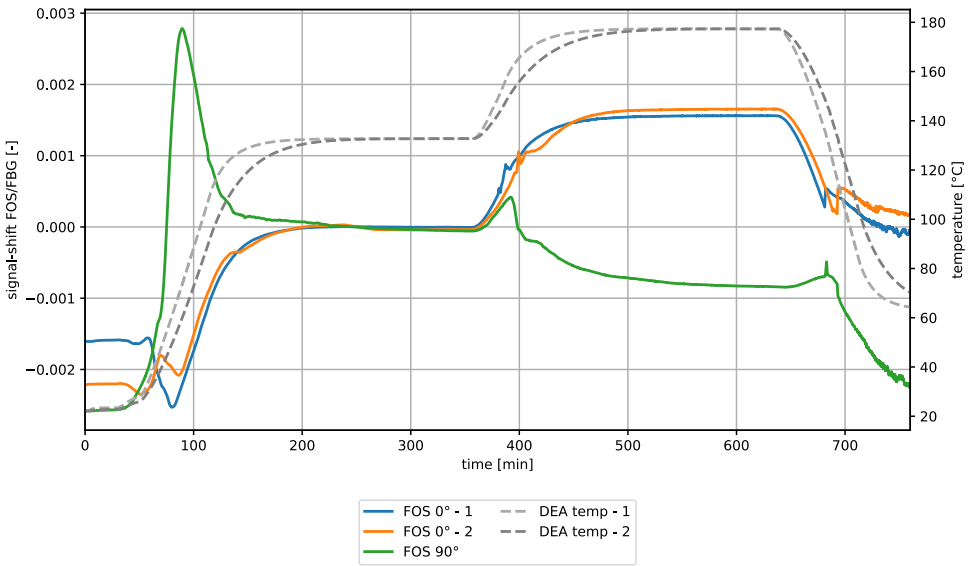

Fig. 22 Signal shift of selected HR-FOS and FBG measurement points over time (tags correlate to Fig. 21)

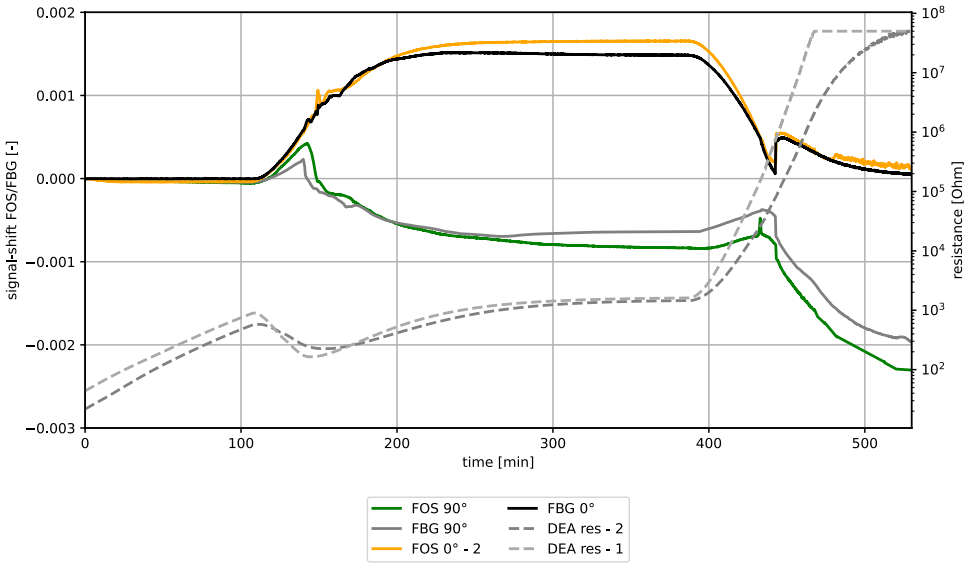

Fig. 23 Detected signals and local similarities of FOS, FBG and DEA (second heat up until cool down) (tags correlate to Fig. 21)

in strain is likely caused by the chemical shrinkage of the resin. The curing reaction induces a transition from a liquid to a rubber-like material, which is accompanied by a significant volume reduction in the resin, resulting in a characteristic strain peak [47]. During this period, the gel point of the resin can be expected [48].

As the degree of cure increases, the interaction between individual laminate layers as well as with the tooling intensifies. In the 0° direction, this interaction appears to prevent the formation of a distinct peak. However, characteristic inhomogeneities are observed in the signal during the assumed gelation phase, suggesting an influence of the material transformation on the measurement signal.

This assumption is further supported by dielectric analysis (DEA) sensors, which detect corresponding variations in laminate resistance, indicating changes in the liquidity and viscosity of the matrix system, as shown in Fig. 23. The plot also includes data from the two FBG sensors alongside the FOS data for 0° (Position 2) and 90° orientation. The data is displayed starting from the first dwell phase, and for comparability, all values are normalized at the beginning. Both the 90° and 0° oriented sensors exhibit similar signals with the same local characteristics.

After curing at 180°C, cooling results in a reduction of strain in the 0° direction. The local strain peaks observed during cooling are most likely caused by the difference in thermal expansion coefficients between CFRP and aluminum tooling (see peaks at 680 min in Fig. 22). During the cooling phase, separation between the laminate and the tool occurs once the strain mismatch between CFRP and aluminum exceeds a critical threshold [49]. In the 90° direction, the interaction appears more complex due to the closed mold configuration and differing cooling rates. Here, both the FOS and FBG sensors detect a local increase in strain. While the laminate is expected to contract due to rapid cooling, the surrounding aluminum tool, with its significantly higher thermal mass, remains warmer and does not contract as quickly as the spar. As long as the laminate remains in contact with the tool, this temperature differential could explain the characteristic strain evolution in the 90° direction.

6.3 Investigation on manufacturing deviations and defects

After and during manufacturing, the resulting spar is examined. This includes evaluation of the sensors within the spar and the mold and evaluation by means of measuring the deviation. In this paper only preliminary results are shown with regards to measuring the deviation.

Each spar is tested for its laminate thickness after curing at eight points. Due to the shape of the mold, this can only be done at its edges. Each spar has a medium thickness about eight measurement points of between 3.03 and 3.07 mm and is therefore well within the limit of 3 ± 0.125 mm.

Optical Measurements of the spar and the spar molds are done with the Zeiss ATOS System. This shows that the mold surface of the lower mold is around 0.3 mm too far away from the parting plane, making the spar thicker.

In Fig. 24 the deviation of the last manufactured spar from the CAD geometry is shown. The measurement is done before trimming the edges so that no induced stresses are relieved. Red colors indicate the actual surface being inside the target geometry, blue indicates the opposite.

Especially on the lower side a big area lies within the target surface. The forward and backwards facing sides on the other hand fit well to the CAD geometry with a deviation of below ±0.05 mm.

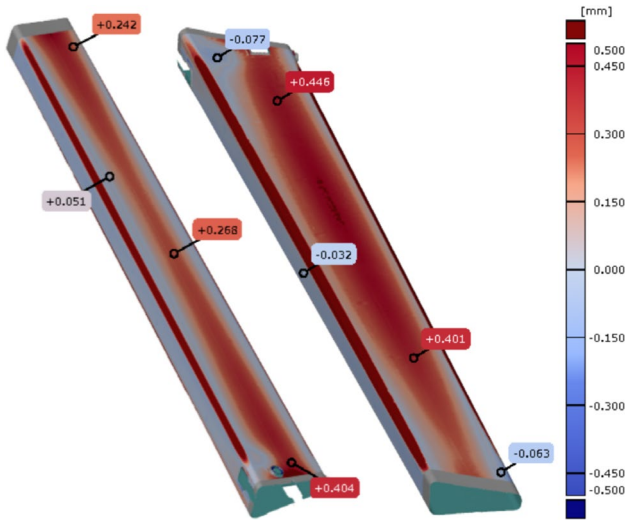

Fig. 24 Deviation of the finished spar with upper side left and lower side right

All corners have a bigger radius compared to the target. This results in a deviation of up to 2 mm with the bigger deviation being again on the lower side. This deviation was already noticed visually while transferring the preform to the mold (see Sect. 6.1). Together with the optical measurement results, a likely cause can be derived. The manufactured corner radius of the mandrel and therefore of the preform is too big. This results in the bigger corner radius. In order for the preform to adapt to the corner radius of the mold during curing, the individual layers would have to slide against each other. This happens to a certain extent as seen by the high peak in 90° direction in Fig. 22, but not enough to fully close the gap. As a result, the circumference of the preform is longer than the one of the mold. Due to the small bending stiffness, the upper and lower surface of the spar buckle inward and then cure in that shape. In the future this can be mitigated by changing the material of the mandrel to hard material like aluminum or PU and by better controlling the tolerances during milling of the mandrel. As already mentioned, pressure strips could reduce the error as well [45]. Furthermore, the type of metal of the mold could be changed. Due to differences in thermal expansion coefficient (CTE) of Aluminium and CFRP, the Aluminium expands more during the heating phase of the curing cycle. While this was considered by scaling the "cold" mold in CAD so that it has the target shape during the curing phase, this only affects dimensional accuracy of the final part. An interaction between other materials like Invar with a CTE similar to CFRP could mitigate the problem with the cost of high material prices [45]. Changing the cure cycle could reduce deviations as well. In [50] an adapted cure cycle for fiber metal laminates was found, which was based on embedded FBG-sensors. Through this, residual thermal stresses could be reduced. In [51] an active control for a thick laminate was introduced, mainly to reduce process times. A simulation model was coupled with temperature measurements and a curing model to achieve this. In [52] an additional neural network model was trained to achieve an even more in-depth real-time control of various curing parameters. Additionally, a friction model was introduced to get knowledge about the interaction between part and mold over various degrees of cure. These examples for changing the curing cycle could reduce the observed manufacturing deviations. If a transfer to the part within this paper can be made is yet unclear.

7 Summary and outlook

In summary, this paper presents the design and development of an aileron for a high-aspect ratio wing with active flutter control. The novel structural concept, adapted from a flap design, is transferred to an aileron, resulting in a highly integrated structural design. A focus is put on understanding and designing the load paths within the aileron and optimizing the location and attachment points for the brackets and stiffeners. Simulation show a high torsional stiffness and deformations within the limits. This deformation is dominated by bending. A stress analysis was done in FEM and with handbook methods, showing a sufficient factor of safety. The spar is manufactured by hand draping the individual layers around a mandrel and subsequent transferring to the mold. Deviations in the tolerances for the mandrel, the preform and the mold result in the radii of the preform not following the mold and therefore resulting in deviations from the target shape. With more detailed analyses, the effects during manufacturing can be further investigated in the future, allowing for a more precise correlation between the strain behavior and the curing process. The use of fiber optical sensors enables strain measurements at a large number of points across the entire component, providing comprehensive structural monitoring with minimal effort, as only a single sensing fiber needs to be integrated. This opens up opportunities for advanced process control, residual stress evaluation and process optimization, ultimately leading to improved manufacturing accuracy and component performance. The concept is suited for modern manufacturing processes with minimal parts count and manufacturing steps. While not shown here, the ailerons' structure is well fitted to a SQRTM process. A weight reduction could be further achieved by refining the layup in local spots, strengthening load introduction points and weakening areas, where loads are less. Further, the brackets could be redesigned in order to not require a double fitment between upper and lower skin. The design and calculations will be evaluated in the

HIL-test stand. This will be part of a future publication. To summarize, this aileron is well suited as a baseline for different studies of a modern generation of ailerons and other moveables.

Acknowledgements This work was funded by the federal ministry for economic affairs and climate action (*Bundesministerium für Wirtschaft und Klimaschutz*) of the German government based on a resolution of the Bundestag. The project WISDOM (Grant No. 20Y2105A) is part of the Federal Aeronautical Research Program (LuFo VI-2). The authors would especially like to thank Konstantin Schmidt for his contribution during manufacturing.

Author Contributions D.S. was responsible for the overall design, simulation and manufacturing of the aileron. Y.B. and R.P. were responsible for the integration and evaluation of the FOS and FBG sensors. R.H. was responsible for the integration and evaluation of the DEA Sensors. N.L. was responsible for the integration and evaluation of the temperature sensors.

Funding Open Access funding enabled and organized by Projekt DEAL. This work was funded by the federal ministry for economic affairs and climate action (Bundesministerium für Wirtschaft und Klimaschutz) of the German government based on a resolution of the Bundestag. The project WISDOM (Grant No. 20Y2105A) is part of the Federal Aeronautical Research Program (LuFo VI-2).

Data availability Manufacturing data can be made available from the corresponding author upon reasonable request. Simulation and geometric data are not available due to confidential material and geometric data.

Code availability Code regarding the BJSFM tool can be made available from the corresponding author upon reasonable request.

Declarations

Competing of Interest The authors declare no Conflict of interest.

Ethical approval and consent to participate Not applicable due to lack of guidelines.

Consent for publication Not applicable due to lack of guidelines.

References

1. Regan, C.D., Jutte, C.V.: Survey of Applications of Active Control Technology for Gust Alleviation and New Challenges for Lighter-weight Aircraft. Technical Report NASA/TM-2012-216008, Dryden Flight Research Center, Edwards, California (2012)
2. McLean, D.: Gust-alleviation control systems for aircraft. In: Proceedings of the Institution of Electrical Engineers, vol. 125, pp. 675–685 (1978). https://doi.org/10.1049/piee.1978.0159. IET
3. Pusch, M., Knoblach, A., Kier, T.: Integrated optimization of ailerons for active gust load alleviation. In: International Forum on Aeroelasticity and Structural Dynamics, St. Petersburg, Russia (2015)
4. Wilke, H., Silva, G., Silvestre, F.: Aileron-flap-integrated roll control law by optimized control allocation for flexible transport aircraft. In: 34th ICAS-Conference, Florence, Italy (2024)
5. Langen, S., Schreppel, C., Stalla, F., Kier, T.M., Wilke, H., Süelözgen, Looye, G.: Development and Integration of Active Load Control Functions for a High Aspect Ratio Transport Aircraft Simulation. In: AIAA SCITECH 2025 Forum. https://doi.org/10.2514/6.2025-1855
6. Fournier, H., Massioni, P., Tu Pham, M., Bako, L., Vernay, R., Colombo, M.: Robust gust load alleviation of flexible aircraft equipped with lidar. J. Guid. Control. Dyn. **45**(1), 58–72 (2022). https://doi.org/10.2514/1.G006084
7. Wallace, C., Schulz, S., Fezans, N., Kier, T., Weber, G.: Evaluation Environment for Cascaded and Partly Decentralized Multi-Rate Load Alleviation Controllers. In: 33rd Congress of the International Council of the Aeronautical Sciences, ICAS 2022, Stockholm, Sweden (2022). https://doi.org/10.60801/ICAS-2022-0656
8. Peytouraux, A.: Proposed Special Condition for Installation of Flutter Suppression System Applicable to Boeing B 747-8F/-8. Accessed 27 Nov 2025 (2011). https://www.easa.europa.eu/en/document-library/product-certification-consultations/proposed-special-condition-installation-1
9. Certification Specifications and Acceptable Means of Compliance for Large Aeroplanes (CS-25). Technical Report Amendment 28, EASA (December 2023)
10. Schumann, H., Lübbe, S., Klimmek, T., Quero, D.: Prüfstand für multifunktionale Flugsteuerungssysteme zur Lastminderung und Flatterunterdrückung bei Verkehrsflugzeugen, Stuttgart (2023). https://doi.org/10.25967/610255. Deutscher Luft- und Raumfahrtkongress
11. Livne, E.: Aircraft active flutter suppression: state of the art and technology maturation needs. J. Aircr. **55**(1), 410–452 (2018). https://doi.org/10.2514/1.C034442
12. Lübbe, S., Bertram, O.: Safety critical Design of Flight Control System Architecture - Potential Safety Aspects for a triple Split Aileron for the Project WISDOM, Stuttgart (2023). https://doi.org/10.25967/610292
13. Griffin, C.F., Dunning, E.G.: Development of an advanced composite aileron for the l-1011 transport aircraft. Technical Report NASA/CR 3517, Lockheed-California Co., Burbank, California (1982)
14. Romano, F., Fiori, J., Mercurio, U.: Structural design and test capability of an cfrp aileron. Compos. Struct. **88**(3), 333–341 (2009). https://doi.org/10.1016/j.compstruct.2008.04.010
15. Breuer, P.U.: Commercial Aircraft Composite Technology, 1st edn. Springer, Kaiserslautern (2016). https://doi.org/10.1007/978-3-319-31918-6
16. Gueuning, D., Mathieu, F.: Evolution in composite injeciton moudling processes for wing control surfaces. SAMPE J. **52**(1) (2016)
17. Ginger, G.: Reducing manufacturing cost via RTM (2015). https://www.compositesworld.com/articles/reducing-manufacturing-cost-via-rtm
18. FACC: "'Wing of Tomorrow"': FACC und Airbus entwickeln Flügel der Zukunft (2021). https://www.facc.com/de/news/wing-of-tomorrow-facc-und-airbus-entwickeln// -fluegel-der-zukunft/

19. Rädel, M., Denker, B., van de Kamp, B., Liebers, N., Prussak, R.: Towards the validation of manufacturing simulations by means of digital twins: conception, implementation and data acquisition for a composite aircraft moveable manufacturing process. CEAS Aeronaut. J. **16**, 399–416 (2025). https://doi.org/10.1007/s13272-024-00800-3
20. Lange, F., Zakrzewski, A.S., Rädel, M., Hollmann, R.W., Risse, K.: Digital Multi-Disciplinary Design Process for Moveables at Virtual Product House. In: Deutscher Luft- und Raumfahrtkongress, Bremen, Germany (2021). https://doi.org/10.25967/550048
21. Rädel, M., Delisle, D.P.P., Krombholz, C., Bertling, D., Hein, R., Wille, T.: Towards Robustness Assessment in Virtual Testing—Manufacturing Influences by Simulation-based Methods in the Virtual Product House, Bremen, Germany (2021). Accessed 21 Nov 2025. https://elib.dlr.de/189104/
22. Hollmann, R.W., Schäfer, A., Bertram, O., Rädel, M.: Virtual Testing of Multifunctional Moveable Actuation Systems at Virtual Product House, Bremen, Germany (2021). Accessed 21 Nov 2025. https://elib.dlr.de/146686/
23. Doeland, W.: Notification of a proposal to issue a certification memorandum: modelling & simulation—CS-25 structural certification specifications. Technical Report EASA Proposed CM No.: CM-S-014 Issue 01. EASA. Accessed 21 Nov 2025. https://www.easa.europa.eu/en/document-library/product-certification-consultations/proposed-certification-memorandum-modelling
24. Airoldi, A., Quarantana, G., Beltramin, A., Sala, G.: Design of a morphing actuated aileron with chiral composite internal structure. Adv. Aircraft Spacecr. Sci. **1**(3), 331–351 (2014). https://doi.org/10.12989/aas.2014.1.3.331
25. Amendola, G., Dimino, I., Concilio, A., Amoroso, F., Pecora, R.: Preliminary design of an adaptive aileron for the next generation of regional aircraft. J. Theor. Appl. Mech. **55**(1), 307–316 (2017). https://doi.org/10.15632/jtam-pl.55.1.307
26. Cavalieri, V., De Gaspari, A., Ricci, S.: Aero-structural design optimization of a morphing aileron considering actuation aspects (2024). https://doi.org/10.2514/6.2024-2113
27. Tikalsky, J.: Hytem demonstrator: design and analysis of a morphing trailing edge demonstrator using hyperelastic adhesive. In: 17th Annual Conference of the Smart Materials, Adaptive Structures and Intelligent Systems, SMASIS 2024, Atlanta, USA (2024). https://doi.org/10.1115/SMASIS2024-140049
28. Smith, J.W., Lock, W.P., Payne, G.A.: Variable-Camber Systems Integration and Operational Performance of the AFTI/F-111 Mission Adaptive Wing. Technical Report Technical Memorandum 4370, NASA (1992)
29. Kota, S., Martins, J.R.R.A.: Flexfloil shape adaptive control surfaces—flight test and numerical results. In: ICAS 2018, Belo Horizonte, Brazil (2018)
30. Barbarino, S., Bilgen, O., Ajaj, R.M., Friswell, M.I., Inman, D.J.: A review of morphing aircraft. J. Intell. Mater. Syst. Struct. **22**(9), 823–877 (2011). https://doi.org/10.1177/1045389X11414084
31. Klimmek, T., Schulze, M., Wöhler, S.: Development of a Short Medium Range Aircraft Configuration for Aeroelastic Investigations using cpacs-MONA, Dresden. Deutscher Luft- und Raumfahrtkongress (2022)
32. Mißbach, M.: Untersuchung eines Bauweisenkonzepts für Landeklappenkörper hochgestreckter Flügel und deren Lasteinleitungsbereiche. Master's thesis, Deutsches Zentrum für Luft- und Raumfahrt e.V., Bremen (2022)
33. Marsh, G.: Composites to the fore at Australian air show. Reinf. Plast. (2007). https://doi.org/10.1016/S0034-3617(07)70215-1
34. Mehmet, F.: TUSA?, Airbus A350'ye yön veriyor. https://www.defenceturk.net/tusas-airbus-a350ye-yon-veriyor. Accessed: 31 July 2024 (2020)
35. Marsh, G.: Automating aerospace composites production with fibre placement. Reinf. Plast. **55**(3), 32–37 (2011). https://doi.org/10.1016/S0034-3617(11)70075-3
36. Properties and Selection: Nonferrous Alloys and Special-Purpose Materials. ASM International, Ohio (1990). https://doi.org/10.31399/asm.hb.v02.9781627081627 . ASM Handbook Committee
37. Thornton, S.T., B., M.J.: Classical Dynamics of Particles and Systems, 5th edn. Brooks Cole, Belmont, USA (2003)
38. Kier, T., Looye, G., Scharpenberg, M., Reijerkerk, M.: Process, methods and tools for flexible aircraft flight dynamics model integration. In: International Forum on Aeroelasticity and Structural Dynamics, Stockholm (2007)
39. ANSYS Inc.: Ansys 2023R2 Mechanical User Guide. Technical report, ANSYS Inc., Pennsylvania (2023)
40. Vasiliev, V.V., Morozov, E.V. (Eds.): Advanced Mechanics of Composite Materials and Structures, Fourth edition edn. Elsevier, Amsterdam (2018). https://doi.org/10.1016/C2016-0-04497-2
41. Garbo, S.P., Ogonowski, J.M.: Effect of variances and manufacturing tolerances on the design strength and life of mechanically fastened composite joints (volume i,ii,iii). Technical Report ADA101657, McDonnel Aircraft Company, McDonnell Douglas Corporation (April 1981)
42. Lekhnitskiy, S.G.: Anisotropic Plates, Moscow (1957). Translated to English under Contract AF33(657)-16408
43. Garbo, S.P.: Design and analysis of composite structures with stress concentrations. Technical Report 19830025689, McDonalld Aircraft Co., St. Louis, Missouri (1983)
44. Wiedemann, J.: Leichtbau - Elemente und Konstruktion, 3rd edn. Springer, Heidelberg (2007). https://doi.org/10.1007/978-3-540-33657-0
45. Lengsfeld, H., Lacalle, J., Neumeyer, T., Altstädt, V.: Composite Technology: Prepregs and Monolithic Part Fabrication Technologies. Hanser eLibrary. Hanser Publications and Hanser Publishers, Munich and Cincinnati (2021)
46. Kratz, J., Mesogitis, T., Skordos, A., Hamerton, I., Partridge, I.: Developing cure kinetics models for interleaf particle toughened epoxies (2016)
47. Prussak, R., Stefaniak, D., Hühne, C., Sinapius, M.: Evaluation of residual stress development in frp-metal hybrids using fiber bragg grating sensors. Prod. Eng. **12**, 259–267 (2018). https://doi.org/10.1007/s11740-018-0793-4
48. Prussak, R., Stefaniak, D., Kappel, E., Hühne, C., Sinapius, M.: Smart cure cycles for fiber metal laminates using embedded fiber bragg grating sensors. Compos. Struct. **213**, 252–260 (2019). https://doi.org/10.1016/j.compstruct.2019.01.079
49. Hein, R., Prussak, R., Schmidt, J.: Phenomenological analysis of thermo-mechanical-chemical properties of gfrp during curing by means of sensor supported process simulation. Processes (2020). https://doi.org/10.3390/pr8020192
50. Prussak, R., Stefaniak, D., Kappel, E., Hühne, C., Sinapius, M.: Smart cure cycles for fiber metal laminates using embedded fiber Bragg grating sensors . Compos. Struct. **213**, 252–260 (2019). https://doi.org/10.1016/j.compstruct.2019.01.079
51. Tifkitsis, K.I., Winistoerfer, A., Skordos, A.A.: Online optimisation and active control of the cure process of thick composite laminates. J. Manuf. Process. **87**, 221–230 (2023). https://doi.org/10.1016/j.jmapro.2023.01.027
52. Tang, W., He, L., Hui, X., Niu, J., Xu, Y., Yang, R., Liu, Y.: Real-time control for autoclave curing process of CFRP composites considering tool-part interaction. Chin. J. Aeronautics (2025). https://doi.org/10.1016/j.cja.2025.103948